Exploring the magnetic properties of W-type $SrFe_{18}O_{27}$ hexaferrite: Insights from a first-principles study

Riyajul Islam [*] and S. P. Madsen [†]
Department of Mechanical and Production Engineering, Aarhus University, Katrinebjergvej 89 G-F, 8200 Aarhus N, Denmark

Mogens Christensen [‡]
Department of Chemistry and Interdisciplinary Nanoscience Center (iNANO), Aarhus University, Gustav Wieds Vej 14, 8000 Aarhus C, Denmark

(Received 10 October 2023; revised 19 November 2023; accepted 22 December 2023; published 12 January 2024)

W-type $SrFe_{18}O_{27}$ hexaferrite is emerging as a potential material for permanent magnet applications. Despite this, theoretical modeling on W-type hexaferrites is still lacking, leaving only experimental findings to date. Employing density functional theory, we conduct a detailed analysis of pure W-type $SrFe_{18}O_{27}$ hexaferrite and its compositions with Ni/Zn substitutions, to explore their intrinsic magnetic properties and assess their viability as potential permanent magnets. We found no significant effect of Ni/Zn substitution on the magnetocrystalline anisotropy energy (MAE); however, Zn substitution is particularly helpful for improving the magnetization $\mu_0 M_s$. The calculated MAE constant K_u values indicate that the compounds are uniaxial with easy axis along the (001) direction. The origin of the predicted MAE is investigated using second-order perturbation theory analysis and the electronic structure. We found that different Fe sublattices contribute differently to the MAE, providing a unique way to enhance the MAE with small site-specific substitutions. The results highlight the challenge of simultaneously enhancing K_u and $\mu_0 M_s$ in W-type hexaferrite compounds. However, the compounds show intriguing properties with moderate K_u and high $\mu_0 M_s$, which may outperform the conventional M-type ferrite magnets in some applications.

DOI: 10.1103/PhysRevB.109.024414

I. INTRODUCTION

The pursuit of new and improved permanent magnets (PMs) is everlasting and is a significant topic of interest in worldwide research today. The use of permanent magnetic materials is becoming increasingly popular among mass-market consumers; including medical equipment, industrial items and a variety of new applications, as well as replacing electromagnets in numerous applications, such as small motors and generators [1–4]. These applications usually require high saturation magnetization $\mu_0 M_s$, elevated Curie temperature T_c, and significant magnetocrystalline anisotropy energy (MAE) constant K_u, often supporting "green" energy conversion technologies. In the current market, Nd-Fe-B and Sm-Co are the two most-widely used PMs that contain rare-earth (RE) elements. However, the rising prices of RE elements observed in recent years have prompted widespread research efforts to develop viable alternative materials for the PM industry, with the objective of minimizing or completely avoiding the use of RE elements [5–7]. While the unparalleled potency of RE magnets is essential for high-performance applications, numerous other applications where magnetic strength demands are less stringent, necessitate a trade-off with other considerations like the cost, stability, processability, etc. [8].

So far, significant efforts have been undertaken to improve the physical and magnetic properties of the RE-free PMs. Several RE-free materials with high magnetization have demonstrated potential as an alternative magnet [9–13]. Since the discovery of M-type hexaferrites, these oxides have received a lot of attention as a prospective permanent magnetic material due to their high magnetization and unique magnetic properties [14–16]. Hexaferrites are well-known hard ferrimagnetic materials that find applications as cost-effective hard PMs in magnetic recording media and as components in high-frequency devices [17–19]. While the M-type hexaferrites are widely employed and its substituted variants serve as common PMs, the W-type hexaferrites, despite possessing higher saturation magnetization than the M type, have yet to find commercial application as PMs. Initial interest in W-type $SrFe_{18}O_{27}$ (SrW) hexaferrite as prospective PM was sparked in 1980 when F. K. Lotgering *et al.* [20] found that W-type $BaFe_{18}O_{27}$ had a 10% greater M_s ($\sim$78 emu/g) and comparable anisotropy field to widely utilized M-type hexaferrites. The potential of W-type hexaferrites for PM applications has since been the subject of much experimental investigations [21–26]. The primary emphasis in research concerning W-type hexaferrites has been on substituted variants, with the aim of improving their magnetic properties, particularly the coercivity. While coercivity is affected by the microstructure, surface effects, defects and inhomogeneity; it is also strongly

[*] r.islam@mpe.au.dk
[†] sma@mpe.au.dk
[‡] mch@chem.au.dk

dependent on the intrinsic uniaxial MAE [27]. The MAE of any material serves as the upper limit for the coercivity, making the material difficult to magnetize or demagnetize by external field [28]. In qualitative terms, the MAE describes the tendency for magnetization in specific directions. In PMs, MAE is an indispensable magnetic property resulting from spin-orbit coupling (SOC). An increase in MAE often leads to higher coercivity, allowing for a rise in maximum energy product $(BH)_{max}$, which is a standard measure for the quality of a PM material [29]. Furthermore, the ability to tune the MAE may lead to widespread applications of W-type hexaferrites. The MAE due to the Fe cations can be altered by replacing the Fe with some suitable substitutions. Although the MAE of SrW is uniaxial and the c axis is the easy axis of magnetization, it is still unclear how the different Fe sublattices contribute to the overall anisotropy since these contributions are challenging to determine experimentally. Hence, first-principles calculations are an excellent and powerful tool for determining the contributions from each sublattice and as a result, identifying suitable substitutions to enhance the overall anisotropy of the SrW hexaferrite. In spite of their substantial presence since their initial report in 1952 [30], and being known to exhibit higher magnetization, these compounds have received relatively little to no first-principles study based on density functional theory (DFT), possibly due to their large and complex unit cell of 92 atoms. A thorough analysis of the electronic structure of SrW hexaferrite would pave the way for describing the magnetic properties, particularly emphasizing the uniaxial MAE.

This paper presents a systematic first-principles density functional theory (DFT) and density functional perturbation theory (DFPT) investigation of the stability, electronic and magnetic properties of $SrFe_{18}O_{27}$ (SrW) and Ni/Zn substituted compositions including $SrNi_2Fe_{16}O_{27}$ (SrNW), $SrZn_2Fe_{16}O_{27}$ (SrZW), and $SrNiZnFe_{16}O_{27}$ (SrNZW). We show that substituting Fe by Zn results in better magnetic properties, especially a large value of magnetization $\mu_0 M_s \sim 0.901$ T is achieved compared to 0.652 T for SrW. A thorough investigation of the uniaxial MAE is also provided. The atomic- and orbital-resolved MAE reveal that not only the trigonal bipyramidal Fe ions but also the octahedral coordinated Fe ions contribute to the uniaxial MAE. Combining the d-orbital resolved MAE with the projected density of states (PDOS), a conceptual picture of uniaxial MAE is also presented. The magnetic properties calculated in this paper are in good agreement with the previous experiments. The paper is organized as follows: After the Introduction, the computational details are presented in Sec. II followed by the results and discussion in Sec. III. The concluding remarks are presented in Sec. IV.

II. COMPUTATIONAL DETAILS

We performed density functional theory (DFT) calculations using the Vienna *ab initio* simulation package (VASP) [31]. The plane-wave basis sets and projector augmented wave (PAW) pseudopotential method were employed to treat the electron-ion interactions [32,33] and the generalized gradient approximation (GGA) was used for the exchange-correlation functional parametrized in the Perdew, Burke, and Ernzerhof (PBE) form [34]. The Hubbard model was used to address the strongly correlated $3d$ electrons in the DFT + U scheme, introduced by Dudarev [35]. In this method, U and J are combined to create the effective parameter $U_{eff} = U - J$. For the sake of clarity, the U_{eff} parameter will be referred to as U throughout this study. Based on the linear response ansatz of Cococcioni *et al.* [36], the U parameter was estimated for the treatment of d-electrons, resulting in a value of $U \approx 3$ eV. The kinetic energy cutoff for plane waves was set to 600 eV. A Γ-centered k-point mesh of $5 \times 5 \times 1$ was used for Brillouin zone sampling. All the atomic positions and lattice structures were fully relaxed to forces below 0.01 eV/Å in the structural relaxation and the electronic iteration was performed with a convergence threshold for the self-consistent loop set to 10^{-6} eV. In VASP, the SOC correction is implemented in a fully relativistic noncollinear mode [37], which allows for a self-consistent estimation of the orbital moment and MAE. In noncollinear calculations, the tetrahedron approach with Blöchl corrections for Brillouin zone integrations [38] and a denser k-point mesh of $12 \times 12 \times 2$ were used, to yield well-converged values for MAE. The methodology was first used to examine the well-studied M-type $SrFe_{12}O_{19}$ hexaferrite to confirm the accuracy of the initial parameters used in our computation. The computed magnetic moment and MAE constant values obtained using the GGA + U scheme with $U = 0$, 3, 4.5, and 5 eV are presented in Table IV of Appendix A, and they are found to be in accordance with earlier theoretical works [39,40].

III. RESULTS AND DISCUSSION

A. Structural analysis

The crystal structure of the so-called W-type $SrFe_{18}O_{27}$ (SrW) hexaferrite with space group $P6_3/mmc$ (No. 194) has been described before [18,41]. The SrW crystal structure, shown in Fig. 1, consists of two formula units of $SrFe_{18}O_{27}$ with fifteen nonequivalent sites in the structure including seven different Fe sublattices: $4e$ tetrahedral (S), $4f_{IV}$ tetrahedral (S) denoted as $4f_1$, $6g$ octahedral (S-S), $4f_{VI}$ octahedral (S) denoted as $4f_2$, $12k$ octahedral (R-S), $4f_{VI}$ octahedral (R) denoted as $4f_3$ and $2d$ bipyramidal (R). The magnetic structure was treated as collinear, with the spin moments of Fe atoms at $4e$, $4f_1$, and $4f_3$ sites being antiparallel to the spin moments of Fe at $6g$, $4f_2$, $12k$, and $2d$ sites [18]. In order to illustrate the site preference of the substituted atoms Ni and Zn, we calculated the total energy in the fully relaxed SrW structure after substituting Fe with Ni and Zn in various Fe sites. Our findings based on the total energy calculations suggest that Zn tends to partially replace Fe on half of each $4e$ and $4f_1$ sites in that order. Ni tends to replace Fe at the two $6g$ sites and one each at the $4f_3$ and $4e$ sites in that sequence. Zn^{2+} ions are known to prefer tetrahedral coordination, whereas Ni^{2+} ions prefer an octahedral environment [22,42]. The site preference is consistent with the recently reported experiment for SrNW and SrZW [24]. Figure 8 of Appendix B shows the Ni/Zn substitutions used.

To understand the effect of Ni/Zn substitution on structural properties, we optimized the atomic positions as well as the volume of the four crystal structures within the space group

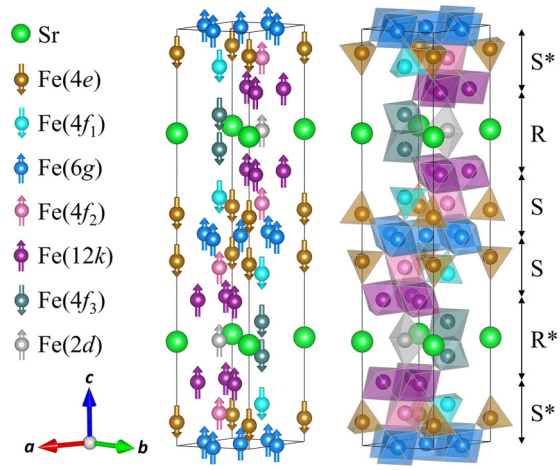

FIG. 1. Crystal structure of W-type $SrFe_{18}O_{27}$ hexaferrite with seven nonequivalent Fe sublattices showing the different spin configurations (left) and crystal structure with colored polyhedral of each Fe sublattices based on their nearest O atoms (right). O atoms are not shown but are located at the corners of the polyhedra. The stacking sequence RSSR*S*S* is also shown with subunits having chemical formulas R = $SrFe_6O_{11}$ (hexagonal) and S = Fe_6O_8 (spinel). The asterisk (*) denotes a 180° rotation of the corresponding subunit around the hexagonal axis.

by minimizing the total energy and atomic forces within the GGA scheme. The computed lattice parameters and volume of the compounds are listed in Table I. The optimized lattice parameters for SrW are slightly smaller than the previously reported experimental values [19,43]. Despite having a greater ionic radius of Ni^{2+} (0.69 Å) than Fe^{3+} (0.64 Å), the lattice constant following Ni substitution reduces when compared to SrW, which is most likely due to defects such as lattice disorders. Moreover, Zn substitution results in an increase in lattice constants with enhanced volume, which is likely due to the slightly larger ionic radius of Zn^{2+} (0.74 Å). The in-plane lattice constant "a" remains nearly unchanged due to the anisotropy of hexagonal systems, where the c axis acts as the easy axis making it easier to align the spins along the c-axis. As a result, there would be significant changes in lattice parameter "c" than in "a," as seen by the results (Table I). It is surprising that the optimized lattice parameters are somewhat underestimated for the experimentally known pure SrW system, despite the well-known tendency of the GGA functional to generally overestimate such parameters. Given that the experiments are carried out at room temperature, it is likely that this discrepancy in our measured values from the experimental values arises due to the thermal expansion of the lattice parameters [44]. However, in the case of Ni/Zn substituted systems, it may also be due to the variation in percentage occupation of Ni/Zn atoms in the various sites, which cannot be replicated precisely with the considered one unit cell.

B. Stability analysis

Next, we investigate the formation enthalpies for the pure SrW and Ni/Zn substituted structures. The formation enthalpy calculations provide important insights into the stability and energetic properties of the systems under study. It is more likely that a system with a lower formation enthalpy will be more stable at higher temperatures. The formation enthalpy H_f of the compounds are calculated, on a per atom basis, based on their phase separation into constituent atoms Sr, Fe, Ni, Zn, and O using the following expression:

$$H_f = \frac{H - \sum_i \mu_i N_i}{N} \tag{1}$$

where H, μ_i, and N are the total energy, chemical potential, and total number of atomic species i, respectively. The computed formation enthalpies for SrW, SrNW, SrZW, and SrNZW are −2.815, −2.741, −2.813, and −2.783 eV/atom respectively. The negative formation enthalpies of all the compounds demonstrate their stability, implying that they are resistant to elemental phase decomposition, i.e., Sr/Fe/Ni/Zn (per atom) in the crystalline form and O_2 in the gas phase. As of now, it has been demonstrated that these compounds can be synthesized in experiments, although with some small secondary impurity phases of M-type and spinel ferrites [19,25,26,43] and that their properties can be controlled with a variety of preparation methods, which will be useful for enhancing their future use as PMs.

We have also examined the dynamical stability of the compounds by calculating the phonon frequencies using the PHONOPY code [45]. The force constants were obtained by density functional perturbation theory (DFPT) approach. In order to determine the accurate phonon frequency, the structures were fully relaxed until the force per atom was less than 0.001 eV/Å and the convergence was performed using 5 × 5 × 1 and denser 12 × 12 × 2 k mesh. Dynamically stable structures must withstand all small perturbations of their atomic structure, resulting in an increase in potential energy. According to the harmonic approximation, this corresponds to all phonons having real frequencies [46]. The computed phonon dispersion band structures of the compounds using 5 × 5 ×

TABLE I. Optimized lattice parameters (Å) and volume (Å^3) in comparison to existing experimental data.

Structure	SrW			SrNW			SrZW			SrNZW		
	$a=b$	c	V	$a=b$	c	V	$a=b$	c	V	$a=b$	c	V
This work	5.877	32.842	982.59	5.835	32.565	960.91	5.894	32.926	990.55	5.878	32.853	983.22
Expt. [19]	5.890	32.774	984.87									
Expt. [43]	5.910	32.844					5.910	32.874	994.42			
Expt. [25]				5.889	32.720		5.901	32.839		5.895	32.792	
Expt. [26]							5.908	32.834				

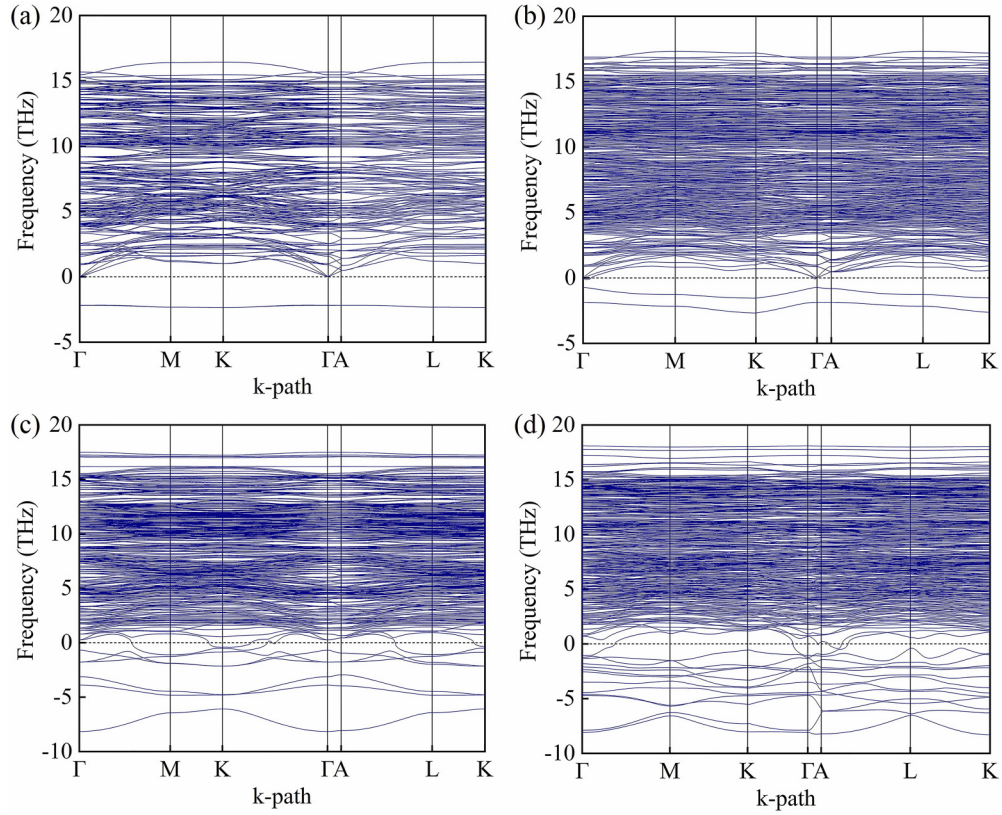

FIG. 2. Phonon dispersion curves along the high symmetry k points of (a) SrW, (b) SrNW, (c) SrZW, and (d) SrNZW. The phonon band structures of the compounds show the existence of imaginary frequencies, indicating their dynamical instability.

1 k mesh are shown in Fig. 2. All the structures reveal the presence of imaginary frequencies with both k-meshes (denoted by negative frequencies in Fig. 2), indicating the dynamical instability of the structures at $T = 0$ K. Imaginary frequencies are observed throughout the whole irreducible Brillouin zone. The imaginary frequencies of the structures do not explain the fact that these structures were experimentally known to occur at high temperatures above $\sim 1100^{\circ}$C [18]. Large atomic displacements are possible at such high temperatures, which may help stabilize the structures and, in such circumstances, the perturbation strategy is invalid. A quantitative explanation necessitates going beyond the harmonic approximation since the imaginary frequencies associated with the dynamic instabilities are inherently anharmonic in nature [47]. Alternative nonperturbative methodologies are necessary in these situations in order to adequately describe the anharmonicity. For phonons with large atomic displacements, the self-consistent phonon method [46,48] and molecular dynamics and lattice dynamics calculations [49] can be applied, which are beyond the scope of this paper.

The formation enthalpy helps forecast the thermodynamic stability of new solid-state compounds [50]; nevertheless, it relates to the formation energies at 0 K. To address the finite temperature effect, which was neglected in the formation enthalpy calculations, the Gibbs free energy can be taken into account. The Gibbs free energy $G(p, T, V)$ as a function of the external pressure p, temperature T, and crystal volume V is given by

$$G(p, T, V) = F_{el}(T, V) + F_{\text{vib}}(T, V) + pV. \tag{2}$$

It is noted that the external pressure throughout the paper is zero and so the last term in Eq. (2) is also zero. Additionally, we employ the harmonic approximation, which has previously proved effective in the investigation of spectroscopic and certain thermodynamic properties of numerous crystals because of its simplicity and predictive capacity [51–54]. The volume dependence of the Gibbs free energy is likewise ignored in this approximation; thus, the Gibbs free energy is solely temperature dependent and is reduced to Helmholtz free energy. In Eq. (2), F_{el} is the electronic Helmholtz free energies and is defined as

$$F_{el}(T) = E(T = 0\ \text{K}) - TS_{el}(T) \tag{3}$$

in which $E(T = 0$ K$)$ is the total energy of the compounds at 0 K obtained from DFT calculations and $TS_{el}(T)$ is the configurational entropy.

F_{vib} is the vibrational free energy due to lattice vibrations, calculated within the harmonic approximation, to the total Helmholtz free energy, which is defined as

$$F_{\text{vib}}(T) = \frac{1}{2}\sum_{\mathbf{q}\nu} \hbar\omega(\mathbf{q}\nu) + k_B T \sum_{\mathbf{q}\nu} ln\left[1 - \exp\left(-\frac{\hbar\omega(\mathbf{q}\nu)}{k_B T}\right)\right] \tag{4}$$

in which $\mathbf{q}$ is the wave vector in the full Brillouin zone, ν is the band index, $\omega(\mathbf{q}\nu)$ is the phonon frequency, and $\hbar$ is the Planck's constant. A direct evaluation of the vibrational

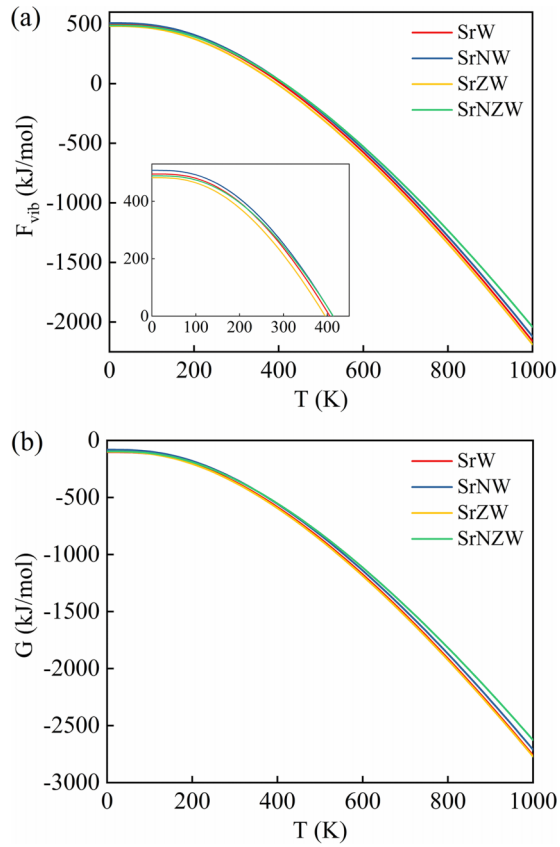

FIG. 3. (a) Computed vibrational Helmholtz free energy F_{vib}, where the inset shows the enlarged view of the F_{vib} and (b) Gibbs free energy G in pure SrW and Ni/Zn substituted compositions.

energy and its effect on thermal properties can be accomplished once the phonon frequencies are computed.

In Fig. 3 we present the vibrational Helmholtz free energy (F_{vib}) and Gibbs free energy (G) as a function of temperature. We can see that all the hexagonal structures have lower negative F_{vib} energies above ∼400 K [Fig. 3(a)] and the Gibbs free energy is overall negative [Fig. 3(b)]. Figure 3 demonstrates that the free energies of the structures have no significant difference at 0 K. However, with increasing temperature, the difference in free energy increases slightly between the structures. Furthermore, the free energy values demonstrate a progressively negative trend as the temperature rises, suggesting that the structures are more thermodynamically stable under realistic conditions favored at higher temperatures.

C. Electronic structure and magnetic moments

In Fig. 4(a), we plot the computed spin-polarized total density of states (TDOS) of the pure and substituted systems within the GGA + U scheme with $U = 3$ eV. The description of 3d electron correlations is improved by the GGA + U scheme. However, one must exercise caution while using the GGA + U scheme for complicated structures since there is a chance that the orbital potential will stabilize an inaccurate electron density. Then, depending on the initial conditions, the method used to include the orbital potential, or different calculation-related parameters (such as the mixing scheme), the computation is caught in a local energy minimum [40]. A gap of 1.496 eV exists in the majority spin channel of pure SrW, while the Fermi level E_F is found within a narrow minimum in the minority spin channel. Upon Ni/Zn substitution, the Fermi level shifts close to the valence band (VB). The Zn substituted system has slightly higher DOS at the Fermi level compared to the Ni substituted system. The projected density of states (PDOS) [Figs. 4(b)–4(h)] of each element (except Sr and O) in different hexaferrite compositions is also examined to determine the significant contributions of each element surrounding the E_F. Sr possesses a stable valency of 2+ with energy levels significantly distant from the E_F. Consequently, while these atoms influence the geometry of the crystal lattice, they have a minimal direct impact on the magnetic properties of the overall compound. Moreover, the Fe-3d and the substituted transition metal (TM) states make up the primary contribution to the TDOS. For all the compounds, the basic characteristics of the DOS results are equivalent. In SrW, the Fe-3d states span about an energy range from −8 to 2.6 eV. In SrNW and SrZW, the Fe-3d states span about the same energy range, extending from −8 to 3.5 eV. Additionally, the Ni-3d and Zn-3d states in SrNW and SrZW span the energy ranges of −7.8 to 2.5 eV and −7.8 to −0.5 eV, respectively. In SrNZW, the Fe-3d states span an energy range from −8 to 3.0 eV, while the Ni and Zn states span about the energy ranges of −7.8 to 2.0 eV and −7.8 to −0.7 eV, respectively. In SrW, the minority spin channel shows the presence of Fe(6g), Fe(4f_2), and Fe(12k) states around the Fermi level. In the considered compounds, all Fe ions are nominally trivalent, while both Ni and Zn are divalent. Substituting Fe^{3+} with Ni^{2+} and Zn^{2+} alters the Coulomb potential, which has immediate ramifications for the properties of the compounds. With the inclusion of Ni in SrNW, the Fe(6g), Fe(4f_2), and Fe(12k) states shift slightly above the Fermi level as compared to SrW. In contrast, the states remain present in SrNZW, whereas only Fe(6g) states are found in SrZW in the minority spin channel. Conversely, the gap observed in the majority spin channel of SrW diminishes upon the addition of Ni, with Ni-3d states appearing near the Fermi level in both SrNW and SrNZW compounds. Our results show that even with higher U values up to 5 eV, all compounds display delocalized solutions in both majority and minority spin channels, with the exception of SrW, which has a larger gap of 1.776 eV for $U = 5$ eV in the majority spin channel and metallic state in the minority spin channel (the TDOS is shown in Fig. 9 of Appendix C). Unfortunately, there are no published experimental or theoretical results available for the pure SrW band gap that could be directly compared with our obtained data.

The spin magnetic moments obtained from our calculations for all compositions are listed in Table II. The Fe cations are often anticipated to be in high-spin states, with spin moments of 4 μ_B or 5 μ_B for Fe^{2+} or Fe^{3+}, respectively. However, despite the small contribution of O-2p states (not shown), it still hybridizes with the neighboring Fe atoms, which significantly lowers the magnetic moments of the Fe atoms. The Ni substitution leads to a small net increase of the magnetic moments by ∼ 2 μ_B. This increase is attributed to the lower spin moments of Ni compared to Fe in the 4e, 6g, and 4f_3 sites, where Ni and Fe exhibit a ferromagnetic arrangement. On the other hand, the substitution of Zn results

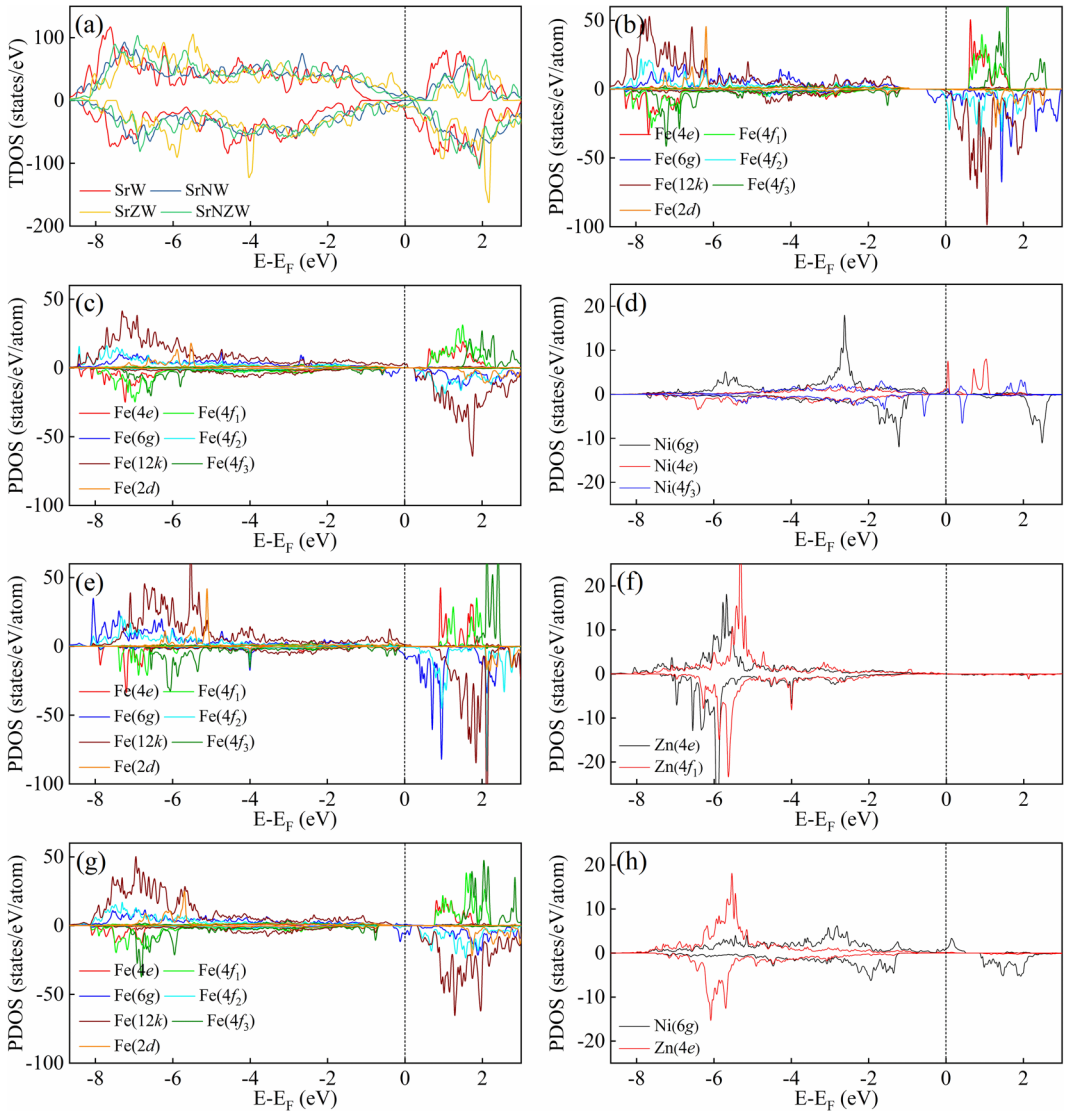

FIG. 4. (a) Comparison of the spin-polarized electronic TDOS for all the considered compounds. Atom projected PDOS contributions to the TDOS for (b) SrW, [(c),–(d)] SrNW, [(e),–(f)] SrZW, and [(g),–(h)] SrNZW compounds. For each plot, the majority spin components align with the positive y axis, while the minority spin components align with the negative y axis. The Fermi level E_F is set at 0 eV.

in a significant increase of net spin magnetic moments, which is due to the reduced average magnetic moments at the 4e and 4f_1 sites (Table II), which are coupled antiferromagnetically to the rest of the Wyckoff sites (except 4f_3). The increase in magnetization may be attributed not only to the substitution of antiferromagnetically coupled Fe(4e) and Fe(4f_1) sites with nonmagnetic Zn atoms (with a spin moment of 0.068 μ_B), but also to the augmentation of ferromagnetism in neighboring Fe(6g) sublattice. The underlying mechanism for this spin moment enhancement lies in the alteration of the spin-polarized PDOS, as shown in Fig. 4. More specifically, the increased magnetic moment of the Fe(6g) atoms can be attributed to the Fe(6g)-3d band shift above the E_F as well as the 3d band narrowing, shown in Fig. 4(e), due to its longer bond lengths with the O atoms $r_{Fe-O} = 2.067$ Å compared to $r_{Fe-O} = 2.056$ Å for SrW. On the other hand, the addition of the Ni atoms has little effect on the neighboring Fe moments. Moreover, the spin splitting of Fe-3d is greater than that of Ni (as shown in Fig. 4), which is consistent with Fe having a larger magnetic moment than Ni. In fact, the local composition has a significant influence on magnetic properties. For SrW and SrZW, our measured total magnetic moments and those obtained from previous experimental measurements are in reasonable agreement [21,23]. Upon comparing the calculated partial magnetic moments for SrNW and SrZW with the previously reported experimental data [24], a reasonable agreement is observed for all sublattices. However, a slight discrepancy exists due to the difference in Ni/Zn substituted occupancies, which was adjusted to make computational cost feasible. Furthermore, the spin magnetic moment results obtained using $U = 0$ and 5 eV are also summarized in Table V of Appendix D. Individual magnetic moments at each site increase significantly from $U = 0$ eV to 5 eV, while the change in overall magnetization is relatively small within ∼0.01 to 0.05 T, except for SrNW with an increase of ∼0.1 T. Our estimated total magnetizations are still greater than those of widely utilized M-type hard ferrites (∼0.40 T) [55–57].

TABLE II. The average total magnetic moments of atoms at each site (μ_B), total magnetic moment m_{tot} per u.c. (μ_B) and saturation magnetizations $\mu_0 M_s$ (T), obtained using $U = 3$ eV. Experimental data (m_{tot} per f.u.) are available only for SrW and SrZW compositions.

Structure	SrW	SrNW	SrZW	SrNZW
Fe($4e$)	−3.950	−3.934	−3.927	−3.946
Fe($4f_1$)	−3.952	−3.948	−3.931	−3.949
Fe($6g$)	3.859	3.856	4.111	3.856
Fe($4f_2$)	4.013	4.089	4.134	4.094
Fe($12k$)	4.104	4.082	4.104	4.114
Fe($4f_3$)	−3.984	−3.976	−3.980	−3.980
Fe($2d$)	3.986	3.976	3.929	3.983
Ni($4e$)		−1.633		
Ni($6g$)		1.539		1.075
Ni($4f_3$)		−0.208		
Zn($4e$)			0.068	0.041
Zn($4f_1$)			0.068	
m_{tot}/u.c.	54.991	56.836	76.586	58.710
m_{tot}/f.u.	27.495	28.418	38.293	29.355
$\mu_0 M_s$	0.652	0.689	0.901	0.696
m_{tot}/f.u. (Expt.)	28.30[a]		35.00[b]	

[a]Reference [23].
[b]Reference [21].

D. Magnetocrystalline anisotropy energy

With a basic understanding of the magnetic moments and electronic structure, we next focus on the estimation of magnetocrystalline anisotropy energy (MAE) constant K_u, which is a key parameter responsible for controlling the coercivity in a magnetic material. MAE is defined as the energy required to orient the spontaneous magnetization M, given by

$$M = M_s(\sin\theta\cos\phi\hat{x} + \sin\theta\sin\phi\hat{y} + \cos\theta\hat{z}) \tag{5}$$

away from easy axis directions with respect to the crystallographic axis under an applied magnetic field. Here, θ is the polar angle between the magnetization vector and the easy axis direction, ϕ is the azimuthal angle between the magnetization component projected onto the a-b plane and the a axis, and $\hat{x}$, $\hat{y}$, and $\hat{z}$ are the unit vectors. For a specific magnet with hexagonal symmetry, the uniaxial anisotropy energy density is formulated as $\frac{E}{V} = K_1\sin^2\theta + K_2\sin^4\theta + K_3\sin^6\theta + ...$, where K_i is the ith order MAE constant [58]. In general, the higher order terms are much smaller than K_1 and K_2, and as a result, when $\theta = \pi/2$, $K_u \approx K_1 + K_2$. The uniaxial MAE constant can then be estimated as the difference in energy density $K_u = \{E(\theta = \pi/2) - E(\theta = 0)\}/V$. We performed self-consistent collinear total energy calculations in the ground state and then incorporated the spin-orbit coupling (SOC) effects non-self-consistently along the (001) and (100) crystallographic directions to predict the MAE constants for the structures. Using the total energy, the MAE constant can similarly be estimated as $K_u = (E_{100} - E_{001})/V$, where V is the unit-cell volume of the structures and $E_{100(001)}$ are the total energy associated with magnetization along the $a(c)$ axis, respectively and are listed in Table III. According to this definition, positive (negative) K_u denotes uniaxial (in-plane) MAE.

The calculated magnetocrystalline anisotropy for the SrW hexaferrite is $K_u = 0.349$ (0.148) MJ/m^3, which is obtained using GGA + SOC (GGA + U + SOC for $U = 3$ eV, as estimated from linear response ansatz), and is roughly of the same order as the experimentally obtained value 0.344 MJ/m^3 [23]. Furthermore, the anisotropy constant obtained for the SrZW structure is 0.394 (0.135) MJ/m^3, using GGA + SOC (GGA + U + SOC for $U = 3$ eV). The predicted K_u result for SrZW differs significantly from the room temperature experimental value of 0.26 MJ/m^3, but the GGA + SOC result supports the low temperature experiment in which K_u = 0.35 MJ/m^3 [21]. Thus, for further analysis of the K_u results, we refer to the results obtained from the GGA + SOC calculations without the U parameter to reduce computational complications. From a theoretical standpoint, we would like to emphasize that direct comparison with the experiment, particularly on the precise magnitude of the MAE constant K_u, should be approached with caution, as an accurate treatment of the d-electron system by first-principles and exact replication of the site occupation by the substituents is quite challenging for such a system with large unit cell as mentioned earlier.

When it comes to analyzing MAE at each sublattice or at the origin, the process is usually not trivial. To elucidate the microscopic origin, the calculated MAE can be analyzed by further decomposing it into contributions from individual sublattices obtained using $\triangle E_{\text{SOC}} = E_{\text{SOC}}^{M\|100} - E_{\text{SOC}}^{M\|001}$. Here, $E_{\text{SOC}}^{M\|100}$ and $E_{\text{SOC}}^{M\|001}$ are the SOC energies with in-plane and out-of-plane magnetization orientation respectively, given by

$$E_{\text{SOC}} = \frac{\hbar^2}{2m^2c^2}\left\langle \frac{1}{r}\frac{dV(r)}{dr}\hat{L}\cdot\hat{S}\right\rangle \tag{6}$$

where $\hat{L}$ and $\hat{S}$ represent orbital and spin angular momentum operators, respectively, while $V(r)$ denotes the spherical part of the effective potential within the PAW sphere. $\triangle E_{\text{SOC}}$ is twice the actual value of the total energy correction associated with the second order, i.e., MAE $\approx \frac{1}{2}\triangle E_{\text{SOC}}$ [59,60]. The

TABLE III. Computed MAE constant K_u (in units of MJ/m^3) in comparison to existing experimental data and magnetic hardness parameter κ. The K_u and κ values are obtained with GGA+SOC (outside parenthesis) and GGA+U+SOC (inside parenthesis for $U = 3$ and 5 eV).

Structure	SrW	SrNW	SrZW	SrNZW
K_u (This paper)	0.349 (0.148, 0.035)	0.130 (0.167, 0.074)	0.394 (0.135, 0.115)	0.339 (0.301, 0.149)
K_u (Expt.)	0.344 (300 K)[a]		0.26 (300 K)[b], 0.35 (6 K)[b]	
κ	1.022 (0.661, 0.322)	0.575 (0.665, 0.472)	0.818 (0.457, 0.418)	0.909 (0.884, 0.618)

[a]Reference [23].
[b]Reference [21].

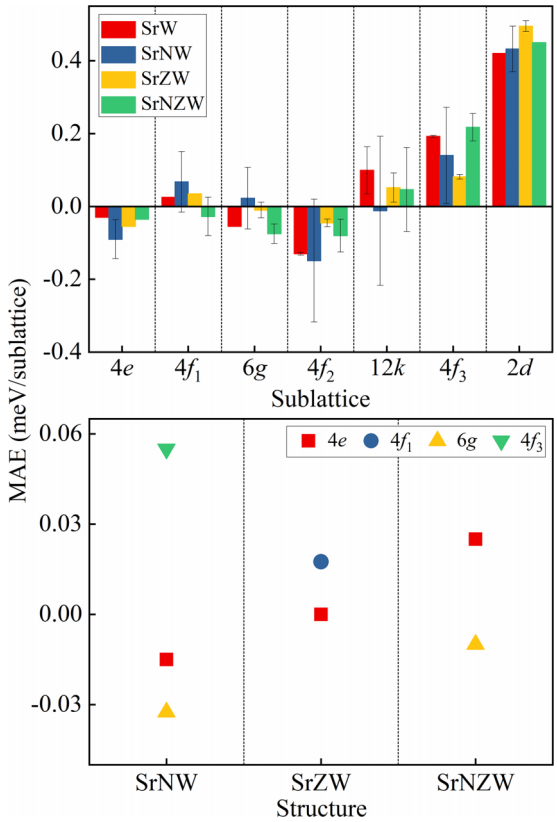

FIG. 5. Calculated sublattice resolved MAE contribution from Fe atoms (top) and Ni/Zn atoms (bottom) to the total MAE constant K_u for pure SrW and Ni/Zn substituted compositions. The values are averaged over the total number of atoms in each sublattice. Column values >0 meV indicate uniaxial anisotropy, while values <0 meV indicate in-plane anisotropy. The error bars indicate the corresponding standard deviation.

remaining half of the SOC energy is converted into crystal-field energy and the formation energy of the unquenched orbital moment [61]. Therefore, using the SOC energies determined for each atom, including the Fe/Ni/Zn atoms, we can evaluate the contribution of a specific sublattice. Figure 5 shows the contribution of average sublattice resolved MAE to the overall K_u for all compositions. It is evident that the single-ion contribution from the Fe-2d bipyramidal site accounts for the predominant contribution to the total K_u. The anisotropic nature of the 2d trigonal bipyramidal site is anticipated due to the geometry of the surrounding five oxygen anions. Large single-ion contributions to the K_u at the 2d bipyramidal site are caused by a strong elongation of the oxygen hexahedron along its local axis, parallel to the easy axis of the unit cell. It should be noted that the trigonal 2d bipyramidal site plays an important role in the anisotropy constant because the ions in this sublattice are strongly perturbed by the unusual five-fold symmetry [62]. Furthermore, in evaluating the MAE per sublattice, the anisotropies observed in the remaining sublattices are nearly an order of magnitude weaker compared to the anisotropy of the Fe-2d sublattice. Nonetheless, their cumulative contributions should not be disregarded due to the larger atom count within each respective sublattice, particularly evident in the case of Fe-12k. The 12k sublattice of SrNW, however, displays a negative contribution in contrast to other structures, which accounts for the lower K_u obtained for SrNW. In addition, when compared to the contributions made by the Fe atoms, the influence of Ni and Zn is notably minuscule in comparison. Further analysis of MAE per sublattice contribution to the total K_u for $U = 3$ and 5 eV is also presented in Fig. 10 of Appendix E. These results support the widely held belief that the anisotropy in hexaferrites results from the combined effects of all other sublattices and not merely the trigonal bipyramidal sublattice [18].

We also computed the d-orbital resolved contribution to the MAE for the Fe sublattices to determine the key parameters influencing the MAE. Due to the weak SOC in 3d based systems, the SOC Hamiltonian can be treated as second-order perturbation and consequently, the energy correction due to the second order SOC, which is the MAE can be estimated as [63]

$$MAE = \xi^2 \sum_{u,o,\sigma,\sigma'} (-1)^{1-\delta_{\sigma\sigma'}} \times \left[\frac{\left|\langle o^{\sigma'}|\hat{L}_z|u^{\sigma}\rangle\right|^2 - \left|\langle o^{\sigma'}|\hat{L}_x|u^{\sigma}\rangle\right|^2}{E_u^{\sigma} - E_o^{\sigma'}} \right] \quad (7)$$

where u^{σ} ($o^{\sigma'}$) and E_u^{σ} ($E_o^{\sigma'}$) denotes the eigenstate and eigenvalue of the unoccupied (occupied) orbitals with $\sigma(\sigma')$ spin states, $\hat{L}_x(\hat{L}_z)$ is the angular momentum operator for the $x(z)$ component, and $\delta_{\sigma\sigma'}$ is the Kronecker delta. As a result, the nonzero SOC matrix components of the $\hat{L}_x$ and $\hat{L}_z$ for the d-orbital contributions to the MAE are $\langle d_{xy}|\hat{L}_x|d_{xz}\rangle = 1$, $\langle d_{x^2-y^2}|\hat{L}_x|d_{yz}\rangle = 1$, $\langle d_{z^2}|\hat{L}_x|d_{yz}\rangle = \sqrt{3}$, $\langle d_{xz}|\hat{L}_z|d_{yz}\rangle = 1$, $\langle d_{x^2-y^2}|\hat{L}_z|d_{xy}\rangle = 2$. In this calculation, we ignore the orbital contributions from the s and p orbitals since their contributions are negligible. Referring to Eq. (7), we analyzed the contributions originating from all possible pairs of d orbitals within the Fe-12k and Fe-2d sublattices (given their prominent contributions to the MAE) and are shown in Fig. 6. Despite minor differences in magnitudes, the fundamental attributes of the d-orbital resolved MAE remain consistent across all the considered compositions. It is evident that the MAE is predominantly influenced by two specific matrix elements., i.e., $\langle d_{z^2}|\hat{L}_x|d_{yz}\rangle$ and $\langle d_{x^2-y^2}|\hat{L}_z|d_{xy}\rangle$. The former matrix element contributes positively to the MAE, indicating that the occupied d_{z^2} orbitals consistently promote uniaxial anisotropy. Conversely, the latter matrix element contributes negatively, implying that the occupied $d_{x^2-y^2}$ orbitals favor planar anisotropy. Moreover, a small uniaxial anisotropy is also produced by $\langle d_{xy}|\hat{L}_x|d_{xz}\rangle$ and $\langle d_{x^2-y^2}|\hat{L}_x|d_{yz}\rangle$, while $\langle d_{xz}|\hat{L}_z|d_{yz}\rangle$ resulted in a small planar anisotropy. Nevertheless, the impact of the uniaxial terms outweighs that of the planar anisotropy terms, resulting in an overall positive MAE. It is worth mentioning that, the MAE may be significantly influenced by SOC induced degenerate band lifting in the nonperturbative scheme and cannot be ruled out entirely [64].

Next, we analyze the d-orbital projected DOS of Fe atoms in 12k and 2d sublattices in SrW to gain a better understanding of the origin of MAE, since these atoms contribute the most to MAE. We confine our investigation to SrW since the contribution from d-orbital resolved MAE is similar for all compositions (as shown in Fig. 6). As depicted in Fig. 7, the

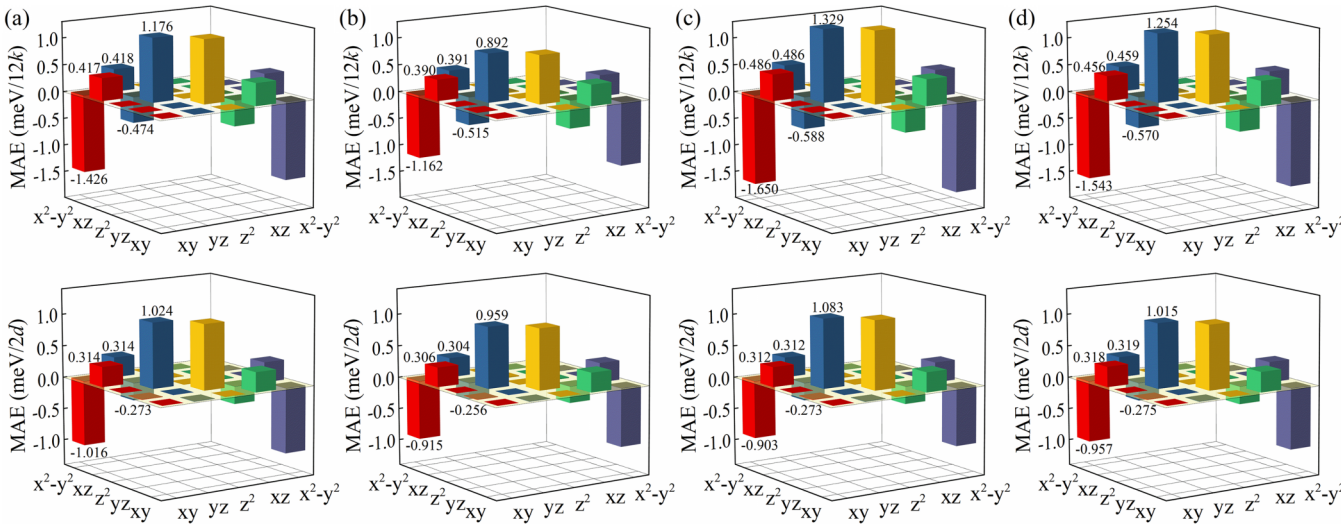

FIG. 6. Calculated average d-orbital resolved MAE for Fe-12k and Fe-2d sublattices in (a) SrW, (b) SrNW, (c) SrZW, and (d) SrNZW. This illustrates how the MAE is affected by the SOC interaction between the various d-orbitals and spin channels. Column values > 0 meV indicate uniaxial anisotropy, while values <0 meV indicate in-plane anisotropy.

majority spin states corresponding to the d orbitals d_{xy}, d_{yz}, d_{z^2}, d_{xz}, and $d_{x^2-y^2}$ are completely occupied, while the minority spin states remain unoccupied. It follows from Eq. (7) that the uniaxial MAE is closely related to the distinct electronic structure around the Fermi level, within which the MAE is primarily governed by the energy difference between the coupling of occupied and unoccupied opposite spin d-orbital pairs. This validates the presence of five SOC matrix elements with positive contribution from the $\langle o\uparrow|\hat{L}_x|u\downarrow\rangle$ matrix elements and negative contribution from the $\langle o\uparrow|\hat{L}_z|u\downarrow\rangle$ matrix elements, as was seen in the earlier description of d-orbital resolved MAE. When the two primary contributors of MAE for SrW are taken into consideration, namely $\langle d_{z^2}|\hat{L}_x|d_{yz}\rangle$ and $\langle d_{x^2-y^2}|\hat{L}_z|d_{xy}\rangle$, the d_{z^2}, d_{yz} and $d_{x^2-y^2}$, d_{xy} orbitals contribute both occupied and unoccupied states, for the majority and minority spin channels respectively, in the vicinity of the Fermi level. For the d_{z^2} and d_{yz} orbital pair, the uniaxial MAE contribution comes from the $\uparrow\downarrow$ coupling between the occupied $d_{yz}\uparrow$ and unoccupied $d_{z^2}\downarrow$ orbitals for 12k and occupied $d_{z^2}\uparrow$ and unoccupied $d_{yz}\downarrow$ orbitals for 2d sublattices,

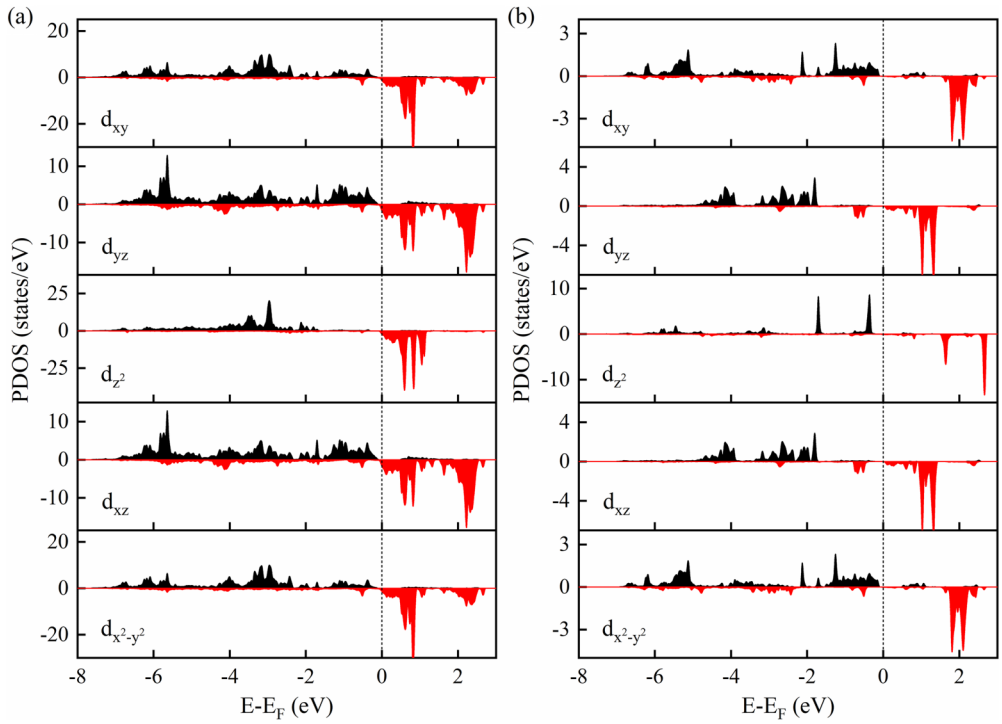

FIG. 7. The d-orbital resolved PDOS of the Fe atoms in (a) 12k and (b) 2d sublattices of SrW. The majority spin components align with the positive y axis, while the minority spin components align with the negative y axis. The Fermi level E_F is set at 0 eV.

TABLE IV. The average total magnetic moments of atoms at each site (μ_B), saturation magnetization $\mu_0 M_s$ (T) and MAE constant K_u (MJ/m^3), obtained using $U = 0$, 3, 4.5, and 5 eV for M-type $SrFe_{12}O_{19}$ hexaferrite in comparison to available experimental data obtained using GGA+U and HSE functionals.

	$U = 0$ eV	$U = 3$ eV	$U = 4.5$ eV	$U = 5$ eV	$U = 4.5$ eV[a]	$U = 3.7$ eV[b]	HSE[b]
Fe($2a$)	3.737	4.095	4.223	4.265	4.20	4.156	4.149
Fe($2b$)	3.543	3.986	4.140	4.190	4.11	4.057	4.044
Fe($12k$)	3.720	4.100	4.226	4.268	4.20	4.170	4.138
Fe($4f_{IV}$)	−3.425	−3.946	−4.115	−4.169	−4.11	−4.038	−4.042
Fe($4f_{VI}$)	−3.155	−3.977	−4.161	−4.217	−4.15	−4.095	−4.093
$\mu_0 M_s$	0.656	0.663	0.667	0.669			
K_u	0.550	0.250	0.206	0.197	0.180	0.190	

[a]Reference [40].
[b]Reference [39].

as can be seen in Figs. 7(a) and 7(b). Furthermore, the energy difference between occupied $d_{x^2-y^2}\uparrow$ and unoccupied $d_{xy}\downarrow$ orbitals is smaller than that of occupied $d_{x^2-y^2}\downarrow$ and unoccupied $d_{xy}\downarrow$, which is clearly visible in case of $12k$ sublattice PDOS [Fig. 7(a)] and hence the $\langle d_{x^2-y^2}\uparrow|\hat{L}_z|d_{xy}\downarrow\rangle$ matrix element is considerably negative. However, despite the large energy difference between $d_{x^2-y^2}\uparrow$ and unoccupied $d_{xy}\downarrow$ orbitals seen in Fig. 7(b), the $2d$ sublattice have notable negative $\langle d_{x^2-y^2}\uparrow|\hat{L}_z|d_{xy}\downarrow\rangle$ matrix element contribution. Considering that the MAE is susceptible to the intensity of the DOS, which integrates across all occupied and unoccupied states, the substantial intensity of the unoccupied $d_{xy}\downarrow$ states around ~ 1.75 eV from the Fermi level can strongly influence the MAE, resulting in a significant negative contribution.

The MAE is essentially derived from SOC, and it may be defined further by taking into account how it depends on the anisotropy of orbital moments. Based on Bruno's model [65], the MAE is often strongly associated with the orbital moment anisotropy Δm_l in systems with a single species, i.e., $MAE = \frac{\xi}{4\mu_B}\Delta m_l$, where ξ denotes the SOC constant and $\Delta m_l = m_l^{M\|001} - m_l^{M\|100}$. The validity of the equation holds solely when considering spin-conserved terms and disregarding spin-flip terms. This theory applies to conventional ferromagnets with substantial exchange splittings, where the majority spin states are predominantly occupied and only minority spin states are close to the Fermi level [66]. The computed total Δm_l values for SrW, SrNW, SrZW, and SrNZW are −0.008, −0.092, −0.013, and 0.02 μ_B respectively. The model anticipates a negative MAE for all structures (except for SrNZW), failing to establish a direct correlation between the MAE and orbital anisotropy. In the considered compounds, the spin-flip terms play a significant role in producing MAE, as was already mentioned in the previous paragraph, while the spin-conserved terms are nonexistent. This phenomenon is responsible for the breakdown of Bruno's relation in these compounds.

A high-performance hard magnetic material should have a magnetic hardness parameter $\kappa = \sqrt{(K_u/(\mu_0 M_s^2)} > 1$, in order to allow fabrication of magnets of any desired shape [1]. The calculated κ values for all compositions are listed in Table III. With the exception of SrW (at $U = 0$ eV), none of the compositions investigated in this study possess the degree of MAE required to attain $\kappa > 1$, due to the higher $\mu_0 M_s$ of the Ni/Zn substituted compounds compared to SrW. Nevertheless, when comparing the higher MAE values for Ni/Zn substituted compounds to those of SrW obtained using $U = 3$ and 5 eV, it is evident that the hardness of these materials exceeds that of SrW, with the exception of SrZW (for $U = 3$ eV). While the MAE found renders it unfeasible to create a hard PM using these compositions, it is, however, adequate to achieve a hardness of $\kappa \sim 0.5$ (for $U = 3$ eV), indicating that these materials can be categorized as semihard materials. As noted by Coey [1], such a semihard magnet would greatly benefit the technology sector, as RE magnets are often used even when a less expensive and lower-performing magnet would suffice.

IV. CONCLUSIONS

In summary, we conducted a combined systematic DFT and DFPT simulations to study the structural stability and the intrinsic magnetic properties of $SrFe_{18}O_{27}$ and Ni/Zn substituted compounds. The formation energies of the compounds demonstrate the feasibility of all compositions to adopt a bulk structure. We compute the phonon dispersions for the pure and Ni/Zn substituted compositions and found negative frequencies throughout the whole Brillouin zone, which indicates all compositions are dynamically unstable. The finite-temperature phase stability was also assessed by

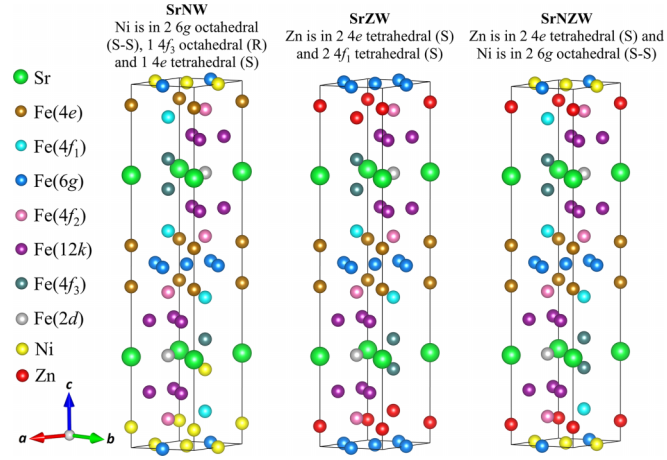

FIG. 8. Crystal structures of SrNW, SrZW, and SrNZW showing different nonequivalent Fe sublattices with Ni/Zn substituted sites.

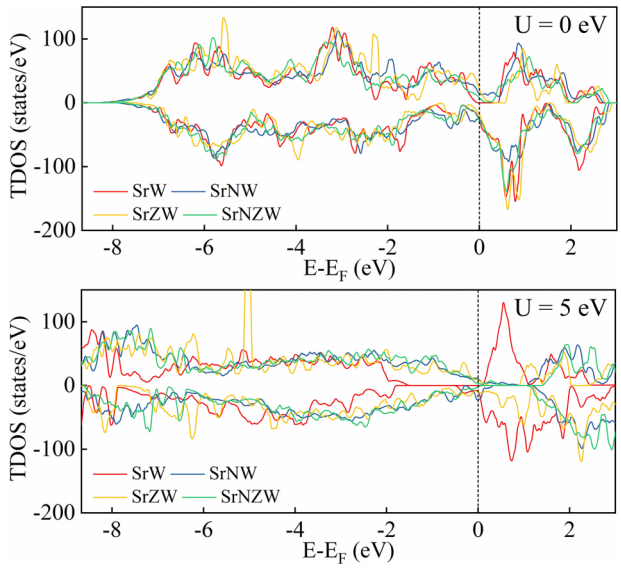

FIG. 9. Spin-polarized TDOS of SrW, SrNW, SrZW, and SrNZW obtained using GGA + U scheme with $U = 0$ and 5 eV.

the vibrational Helmholtz free energy (F_{vib}) and Gibbs free energy (G) within the harmonic approximation. These results suggest that the structures are more thermodynamically stable at higher temperatures under realistic conditions. While we find that Ni/Zn substitution has no favorable effect on the MAE of $SrFe_{18}O_{27}$, for $SrZn_2Fe_{16}O_{27}$, we show that the magnetization can be significantly improved ($\mu_0 M_s = 0.901$ T). A uniaxial MAE of $K_u = 0.349, 0.130, 0.394, 0.339$ MJ/m^3 was calculated for $SrFe_{18}O_{27}$, $SrNi_2Fe_{16}O_{27}$, $SrZn_2Fe_{16}O_{27}$, and $SrNiZnFe_{16}O_{27}$ respectively with the theoretically optimized crystal structures. MAE and atomic magnetic anisotropy are strongly correlated due to spin-orbit coupling. Based on computations of the individual Fe sublattices' contributions to the overall MAE, we find that the 12k and 2d sublattices contribute the most to the MAE. Using second-order perturbation calculations, we confirmed that the uniaxial MAE in $SrFe_{18}O_{27}$ is due to spin-flip perturbation processes around the Fermi level. We discovered the orbital pairings that have a large influence on the MAE and showed that altering the orbital mixing is an effective method for tuning the MAE. These results provide the foundation for $SrFe_{18}O_{27}$ and its substituted variants as promising candidates for rare-earth-free permanent magnets. Nonetheless, there remains potential for enhancing the uniaxial MAE. To enhance the MAE, increasing magnetic anisotropy locally through orbital moment contribution or structural changes is crucial. Cation substitutions are pivotal, particularly by introducing magnetic ions with significant SOC energy contributions. Additionally, replacing Sr^{2+} ions with nonmagnetic or rare-earth ions can modify the crystal structure, potentially influencing the MAE, making cation substitutions a versatile strategy for boosting magnetic materials. We hope that our present study may inspire future experimental and theoretical investigations to improve the MAE, leading to the practical realization of W-type hexaferrite permanent magnets.

ACKNOWLEDGMENTS

This work is supported by the Independent Research Fund Denmark - Green Transitions COMPASS project (1127-00235B). Computational resources are provided by DeiC National HPC (g.a. DeiC-AU-N2-2023011 and DeiC-AU-L5-0010).

APPENDIX A: DFT RESULTS FOR M-TYPE $SrFe_{12}O_{19}$ HEXAFERRITE

In Table IV we compare the magnetic moment and MAE constant K_u results for M-type $SrFe_{12}O_{19}$ hexaferrite with the available theoretical results in order to validate the accuracy of the initial parameters used in our computation. Here we can see that the findings produced with $U = 4.5$ and 5 eV are in reasonable agreement with the known theoretical results, which verifies the calculation methodologies employed in our paper.

TABLE V. The average total magnetic moments of atoms at each site (μ_B), total magnetic moment m_{tot} per u.c. (μ_B) and saturation magnetizations $\mu_0 M_s$ (T), obtained using $U = 0$ and 5 eV.

Strcuture	SrW		SrNW		SrZW		SrNZW	
	$U = 0$ eV	$U = 5$ eV	$U = 0$ eV	$U = 5$ eV	$U = 0$ eV	$U = 5$ eV	$U = 0$ eV	$U = 5$ eV
Fe(4e)	−3.449	−4.189	−3.420	−4.160	−3.444	−4.103	−3.448	−4.157
Fe(4f_1)	−3.437	−4.182	−3.462	−4.173	−3.454	−4.112	−3.381	−4.167
Fe(6g)	3.595	3.986	3.532	4.009	3.816	4.235	3.377	3.977
Fe(4f_2)	3.674	4.211	3.559	4.277	3.856	4.241	3.733	4.284
Fe(12k)	3.714	4.263	3.128	4.102	3.683	4.233	3.736	4.276
Fe(4f_3)	−3.199	−4.219	−3.191	−4.213	−3.169	−4.167	−3.192	−4.216
Fe(2d)	3.553	4.189	3.454	4.175	3.519	4.111	3.550	4.186
Ni(4e)			−1.302	−1.728				
Ni(6g)			1.283	1.651			0.540	1.171
Ni(4f_3)			−0.752	−1.540				
Zn(4e)					0.076	0.060	0.037	0.031
Zn(4f_1)					0.072	0.061		
m_{tot}/u.c.	54.670	55.172	44.652	53.317	73.070	77.412	55.934	59.177
$\mu_0 M_s$	0.648	0.655	0.542	0.647	0.860	0.911	0.664	0.702

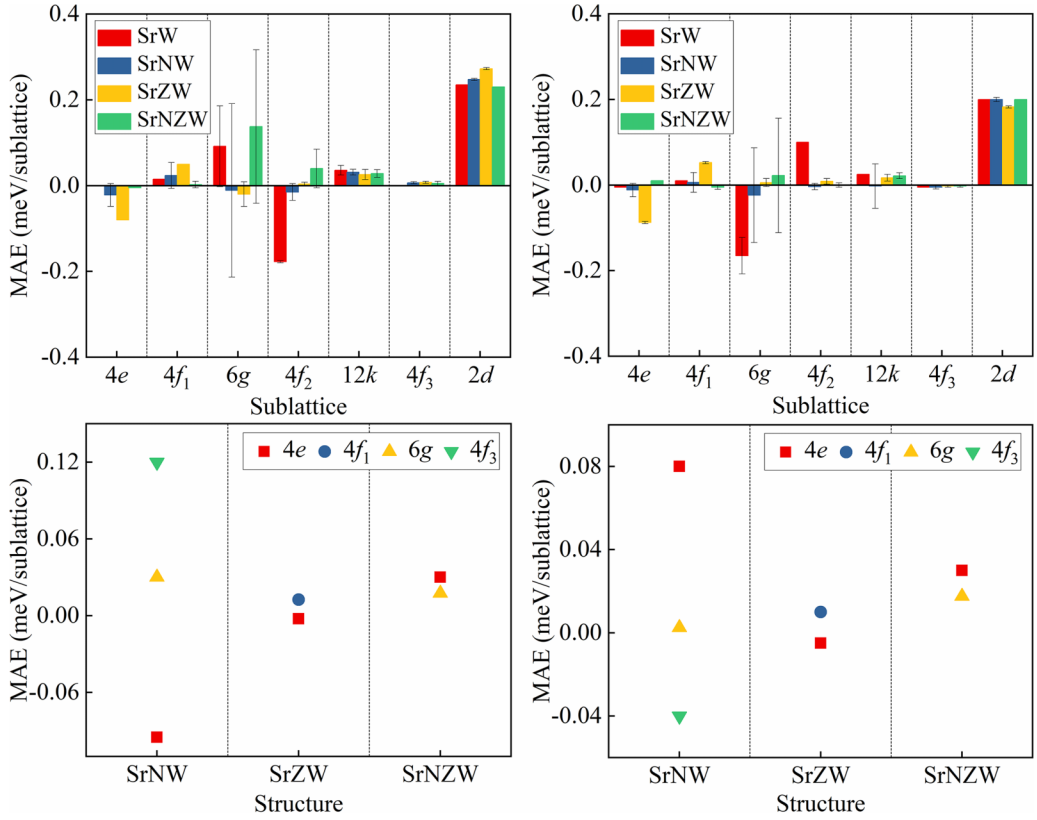

FIG. 10. Calculated sublattice resolved MAE contribution from Fe atoms (top) and Ni/Zn atoms (bottom) to the total MAE constant K_u for pure SrW and Ni/Zn substituted compositions obtained using $U = 3$ eV (left) and 5 eV (right).

APPENDIX B: CRYSTAL STRUCTURES OF SrNW, SrZW, AND SrNZW

The crystal structures of the Ni/Zn substituted compounds SrNW, SrZW, and SrNZW are shown in Fig. 8. The structures distinctly highlight the specific sites where Ni/Zn atoms are substituted. The uniaxial magnetic ordering of the Ni/Zn atoms is identical to that of the Fe atoms.

APPENDIX C: TOTAL DENSITY OF STATES OF PURE SrW AND ITS Ni/Zn SUBSTITUTED COMPOSITIONS

Here we compare the spin-polarized TDOS, shown in Fig. 9, for pure SrW and Ni/Zn substituted compositions within the GGA + U scheme with $U = 0$ and 5 eV. The computed TDOS for SrW shows a small band gap of 0.457 eV for $U = 0$ eV and a large band gap of 1.776 eV for $U = 5$ eV in the majority spin channel while the TDOS occupies the Fermi level in the minority spin channel. However, no plausible gap is observed in both spin directions for the Ni/Zn substituted compositions, as visible in the figure.

APPENDIX D: MAGNETIC MOMENTS OBTAINED USING $U = 0$ AND 5 eV

In Table V, we present the spin magnetic moments of pure SrW and Ni/Zn substituted compositions (SrNW, SrZW and SrNZW) obtained using $U = 0$ and 5 eV.

APPENDIX E: MAE PER SUBLATTICE OBTAINED USING $U = 3$ AND 5 eV

Here we present the average sublattice resolved MAE contribution to the overall K_u for pure SrW and Ni/Zn substituted compositions within the GGA + U scheme with $U = 3$ and 5 eV, is shown in Fig. 10. The computed results also show somewhat similar behavior as in the case of $U = 0$ eV, as explained before, with the predominant contribution coming from the 12k and 2d sites although with somewhat lower magnitude. In contrast, the contributions from the 6g site appear to change sign in the cases of SrNW and SrNZW.

[1] J. M. D. Coey, Permanent magnets: Plugging the gap, Scr. Mater. **67**, 524 (2012).

[2] L. H. Lewis and F. Jiménez-Villacorta, Perspectives on permanent magnetic materials for energy conversion and power generation, Metall. Mater. Trans. A **44**, 2 (2013).

[3] J. Cui, M. Kramer, L. Zhou, F. Liu, A. Gabay, G. Hadjipanayis, B. Balasubramanian, and D. Sellmyer, Current progress and future challenges in rare-earth-free permanent magnets, Acta Mater. **158**, 118 (2018).

[4] I. Matsuzaki, M. Hattori, H. Yamauchi, N. Goto, Y. Iwata, T. Yokoi, M. Tsunemi, M. Kobayashi, T. Yamamura, and

R. Miyahara, Magnetic anchor-guided endoscopic submucosal dissection for colorectal tumors (with video), Surg. Endosc. **34**, 1012 (2020).

[5] S. Sugimoto, Current status and recent topics of rare-earth permanent magnets, J. Phys. D **44**, 064001 (2011).

[6] O. Gutfleisch, M. A. Willard, E. Brück, C. H. Chen, S. G. Sankar, and J. P. Liu, Magnetic materials and devices for the 21st century: Stronger, lighter, and more energy efficient, Adv. Mater. **23**, 821 (2011).

[7] R. W. McCallum, L. Lewis, R. Skomski, M. J. Kramer, and I. E. Anderson, Practical aspects of modern and future permanent magnets, Annu. Rev. Mater. Res. **44**, 451 (2014).

[8] C. C. Pavel, C. Thiel, S. Degreif, D. Blagoeva, M. Buchert, D. Schüler, and E. Tzimas, Role of substitution in mitigating the supply pressure of rare earths in electric road transport applications, Sustain. Mater. Technol. **12**, 62 (2017).

[9] S. Fukami, H. Sato, M. Yamanouchi, S. Ikeda, and H. Ohno, CoNi films with perpendicular magnetic anisotropy prepared by alternate monoatomic layer deposition, Appl. Phys. Express **6**, 073010 (2013).

[10] M. H. Han, W. J. Kim, E. K. Lee, H. Kim, S. Lebègue, and J. J. Kozak, Theoretical study of the microscopic origin of magnetocrystalline anisotropy in $Fe_{16}N_2$ and its alloys: Comparison with the other $L1_0$ alloys, J. Phys.: Condens. Matter **32**, 035801 (2020).

[11] L.-Y. Tian, O. Eriksson, and L. Vitos, Pressure effect on the order-disorder transformation in $L1_0$ FeNi, Sci. Rep. **10**, 14766 (2020).

[12] A. Urru and A. Dal Corso, Lattice dynamics effects on the magnetocrystalline anisotropy energy: Application to MnBi, Phys. Rev. B **102**, 115126 (2020).

[13] L. Yin, R. Juneja, L. Lindsay, T. Pandey, and D. S. Parker, Semihard iron-based permanent-magnet materials, Phys. Rev. Appl. **15**, 024012 (2021).

[14] H. Kojima, Fundamental properties of hexagonal ferrites with magnetoplumbite structure, in *Handbook of Ferromagnetic Materials* Vol. 3, edited by E. P. Wohlfarth (North-Holland Publishing, Amsterdam, 1982) Chap. 5, pp. 305–391.

[15] M. Sugimoto, The past, present, and future of ferrites, J. Am. Ceram. Soc. **82**, 269 (1999).

[16] V. G. Harris, Modern microwave ferrites, IEEE Trans. Magn. **48**, 1075 (2012).

[17] S. Ruan, B. Xu, H. Suo, F. Wu, S. Xiang, and M. Zhao, Microwave absorptive behavior of ZnCo-substituted W-type Ba hexaferrite nanocrystalline composite material, J. Magn. Magn. Mater. **212**, 175 (2000).

[18] R. C. Pullar, Hexagonal ferrites: A review of the synthesis, properties and applications of hexaferrite ceramics, Prog. Mater. Sci. **57**, 1191 (2012).

[19] J. H. You and S. I. Yoo, Improved magnetic properties of Zn-substituted strontium W-type hexaferrites, J. Alloys Compd. **763**, 459 (2018).

[20] F. K. Lotgering, P. H. G. M. Vromans, and M. A. H. Huyberts, Permanent-magnet material obtained by sintering the hexagonal ferrite $W = BaFe_{18}O_{27}$, J. Appl. Phys. **51**, 5913 (1980).

[21] H. Graetsch, F. Haberey, R. Leckebusch, M. Rosenberg, and K. Sahl, Crystallographic and magnetic investigation on W-type-hexaferrite single crystals in the solid solution series $SrZn_{2-x}Co_xFe_{16}O_{27}$, IEEE Trans. Magn. **20**, 495 (1984).

[22] S. Ram and J. Joubert, Synthesis and magnetic properties of $SrZn_2$-W type hexagonal ferrites using a partial $2Zn^{2+} \rightarrow Li^{+}Fe^{3+}$ substitution: A new series of permanent magnets materials, J. Magn. Magn. Mater. **99**, 133 (1991).

[23] H. Ueda, H. Shakudo, H. Santo, Y. Fujii, C. Michioka, and K. Yoshimura, Magnetocrystalline anisotropy of single crystals of M-, X-, and W-type strontium hexaferrites, J. Phys. Soc. Jpn. **87**, 104706 (2018).

[24] M. I. Mørch, J. V. Ahlburg, M. Saura-Múzquiz, A. Z. Eikeland, and M. Christensen, Structure and magnetic properties of W-type hexaferrites, IUCrJ **6**, 492 (2019).

[25] C. G. Knudsen, M. I. Mørch, and M. Christensen, Texture formation in W-type hexaferrite by cold compaction of non-magnetic interacting anisotropic shaped precursor crystallites, Dalton Trans. **52**, 281 (2023).

[26] M. I. Mørch and M. Christensen, Controlling the magnetic structure in W-type hexaferrites, J. Appl. Crystallogr. **56**, 597 (2023).

[27] F. Hellman, A. Shapiro, E. Abarra, P. Rooney, and M. Tran, Magnetic anisotropy and coercivity in magneto-optical recording materials, J. Mag. Soc. **23**, S1_79 (1999).

[28] H. Kronmüller, Theory of Nucleation Fields in Inhomogeneous Ferromagnets, Physica Status Solidi (b) **144**, 385 (1987).

[29] S. Chikazumi, *Physics of Ferromagnetism* (Oxford University Press, Oxford, 1997).

[30] J. J. Went, G. W. Rathenau, E. W. Gorter, and G. W. van Oosterhout, Ferroxdure, A class of new permanent magnet materials, Philips Tech. Rev. **13**, 194 (1952).

[31] G. Kresse and J. Furthmüller, Efficient iterative schemes for ab initio total-energy calculations using a plane-wave basis set, Phys. Rev. B **54**, 11169 (1996).

[32] P. E. Blöchl, Projector augmented-wave method, Phys. Rev. B **50**, 17953 (1994).

[33] G. Kresse and D. Joubert, From ultrasoft pseudopotentials to the projector augmented-wave method, Phys. Rev. B **59**, 1758 (1999).

[34] J. P. Perdew, K. Burke, and M. Ernzerhof, Generalized gradient approximation made simple, Phys. Rev. Lett. **77**, 3865 (1996).

[35] S. L. Dudarev, G. A. Botton, S. Y. Savrasov, C. J. Humphreys, and A. P. Sutton, Electron-energy-loss spectra and the structural stability of nickel oxide: An LSDA+U study, Phys. Rev. B **57**, 1505 (1998).

[36] M. Cococcioni and S. de Gironcoli, Linear response approach to the calculation of the effective interaction parameters in the LDA+U method, Phys. Rev. B **71**, 035105 (2005).

[37] D. Hobbs, G. Kresse, and J. Hafner, Fully unconstrained noncollinear magnetism within the projector augmented-wave method, Phys. Rev. B **62**, 11556 (2000).

[38] P. E. Blöchl, O. Jepsen, and O. K. Andersen, Improved tetrahedron method for Brillouin-zone integrations, Phys. Rev. B **49**, 16223 (1994).

[39] L. S. Liyanage, S. Kim, Y. K. Hong, J. H. Park, S. C. Erwin, and S. G. Kim, Theory of magnetic enhancement in strontium hexaferrite through Zn-Sn pair substitution, J. Magn. Magn. Mater. **348**, 75 (2013).

[40] V. Chlan, K. Kouřil, K. Uličná, H. Štěpánková, J. Töpfer, and D. Seifert, Charge localization and magnetocrystalline anisotropy in La, Pr, and Nd substituted Sr hexaferrites, Phys. Rev. B **92**, 125125 (2015).

[41] P. B. Braun, The Crystal Structures of a New group of ferromagnetic compounds, Philips Res. Rep. **12**, 491 (1957).
[42] M. Iqbal, W. Tahir, G. Murtaza Rai, N. Noor, S. Ali, and K. Kubra, An investigation of the titanium effect on the structural and magnetic properties of $BaNi_2$ based W-type hexaferrites, Ceramics Intl. **38**, 3757 (2012).
[43] T. Reimann, T. Schmidt, and J. Töpfer, Phase stability and magnetic properties of $SrFe_{18}O_{27}$ W-type hexagonal ferrite, J. Am. Ceram. Soc. **103**, 324 (2020).
[44] C. Bhandari and D. Paudyal, Enhancing stability and magnetism of $ThMn_{12}$-type cerium-iron intermetallics by site substitution, Phys. Rev. Res. **4**, 023012 (2022).
[45] A. Togo and I. Tanaka, First principles phonon calculations in materials science, Scr. Mater. **108**, 1 (2015).
[46] D. C. Wallace, *Thermodynamics of Crystals*, Dover books on physics (Dover Publications, New York, 1998).
[47] I. Pallikara, P. Kayastha, J. M. Skelton, and L. D. Whalley, The physical significance of imaginary phonon modes in crystals, Electron. Struct. **4**, 033002 (2022).
[48] I. Errea, M. Calandra, and F. Mauri, Anharmonic free energies and phonon dispersions from the stochastic self-consistent harmonic approximation: Application to platinum and palladium hydrides, Phys. Rev. B **89**, 064302 (2014).
[49] T. Sun, D.-B. Zhang, and R. M. Wentzcovitch, Dynamic stabilization of cubic CaSiO3 perovskite at high temperatures and pressures from *ab initio* molecular dynamics, Phys. Rev. B **89**, 094109 (2014).
[50] V. Stevanović, S. Lany, X. Zhang, and A. Zunger, Correcting density functional theory for accurate predictions of compound enthalpies of formation: Fitted elemental-phase reference energies, Phys. Rev. B **85**, 115104 (2012).
[51] F. Pascale, C. M. Zicovich-Wilson, R. Orlando, C. Roetti, P. Ugliengo, and R. Dovesi, Vibration frequencies of $Mg_3Al_2Si_3O_{12}$ pyrope. An ab initio study with the CRYSTAL code, J. Phys. Chem. B **109**, 6146 (2005).
[52] A. Erba, S. Casassa, R. Dovesi, L. Maschio, and C. Pisani, Periodic density functional theory and local-MP2 study of the librational modes of Ice XI, J. Chem. Phys. **130**, 074505 (2009).
[53] C. Carteret, M. De La Pierre, M. Dossot, F. Pascale, A. Erba, and R. Dovesi, The vibrational spectrum of $CaCO_3$ aragonite: A combined experimental and quantum-mechanical investigation, J. Chem. Phys. **138**, 014201 (2013).
[54] J. Kaczkowski and I. Płowaś-Korus, The vibrational and thermodynamic properties of $CsPbI_3$ polymorphs: An improved description based on the SCAN meta-GGA functional, J. Phys. Chem. Lett. **12**, 6613 (2021).
[55] B. T. Shirk and W. R. Buessem, Temperature dependence of Ms and K1 of $BaFe_{12}O_{19}$ and $SrFe_{12}O_{19}$ single crystals, J. Appl. Phys. **40**, 1294 (1969).
[56] J. M. D. Coey, Hard magnetic materials: A perspective, IEEE Trans. Magn. **47**, 4671 (2011).
[57] R. Skomski and J. M. D. Coey, Magnetic anisotropy — How much is enough for a permanent magnet?, Scr. Mater. **112**, 3 (2016).
[58] R. Skomski, *Simple Models of Magnetism* (Oxford University Press, New York, 2008) p. 336.
[59] V. Antropov, L. Ke, and D. Åberg, Constituents of magnetic anisotropy and a screening of spin-orbit coupling in solids, Solid State Commun. **194**, 35 (2014).
[60] J. Zhang, P. V. Lukashev, S. S. Jaswal, and E. Y. Tsymbal, Model of orbital populations for voltage-controlled magnetic anisotropy in transition-metal thin films, Phys. Rev. B **96**, 014435 (2017).
[61] R. Skomski, A. Kashyap, and A. Enders, Is the magnetic anisotropy proportional to the orbital moment? J. Appl. Phys. **109**, 07E143 (2011).
[62] C. A. M. van den Broek and A. L. Stuijts, Ferroxdure, Philips Tech. Rev. **37**, 157 (1977).
[63] D.-S. Wang, R. Wu, and A. J. Freeman, First-principles theory of surface magnetocrystalline anisotropy and the diatomic-pair model, Phys. Rev. B **47**, 14932 (1993).
[64] A. Lessard, T. H. Moos, and W. Hübner, Magnetocrystalline anisotropy energy of transition-metal thin films: A nonperturbative theory, Phys. Rev. B **56**, 2594 (1997).
[65] P. Bruno, Tight-binding approach to the orbital magnetic moment and magnetocrystalline anisotropy of transition-metal monolayers, Phys. Rev. B **39**, 865 (1989).
[66] K. Masuda, H. Itoh, Y. Sonobe, H. Sukegawa, S. Mitani, and Y. Miura, Interfacial giant tunnel magnetoresistance and bulk-induced large perpendicular magnetic anisotropy in (111)-oriented junctions with fcc ferromagnetic alloys: A first-principles study, Phys. Rev. B **103**, 064427 (2021).